Formulation and Multiobjective Design Optimization of Wound-Field Flux Switching Machines for Wind Energy Drives

Udochukwu B. Akuru, *Member, IEEE*, and Maarten J. Kamper, *Senior Member, IEEE*

***Abstract*—In this study, constrained multiobjective design optimization (MDO) of wound-field flux switching machines (WF-FSMs) for wind energy drives is undertaken in two-dimensional (2-D) static finite-element analyses (FEA), facilitated by simple analytic formulations. The MDO implementation is fully discussed, whereby the simulations for two different problem formulations produce Pareto optimal solutions, which enable important design considerations. Two optimal design candidates, each from the MDO problems investigated, are isolated and compared. The comparison shows that minimizing manufacturing costs places too much pressure on the electromagnetic performance of the WF-FSM, whereas optimizing the generator performance may improve the efficiency and cost of the drivetrain solid state converters (SSCs), with little compromise to the generator costs. In the end, 3-D transient FEA results are provided for validation.**

***Index Terms*—Finite-element analyses (FEA), multiobjective design optimization (MDO), Pareto optimal front/set, solid-state converters (SSCs), wind energy drives, wound-field flux switching machine (WF-FSM).**

I. Introduction

MOSTLY driven by technological revolution and levelized cost of energy reductions in recent times, wind power is becoming established as the leading source of renewable energy for electricity demand [1]. Similarly, electrical machines, which are a major component in wind energy drives, have attracted corresponding attention, both from researchers and the industry [2]–[5]. The commonest electrical machines in use for wind energy drives are doubly fed induction generators (DFIGs) and permanent magnet synchronous generators (PMSGs). Although DFIGs and PMSGs have become established for wind applications, the former are notorious for high maintenance costs, whereas the issue with the latter is the high cost of high-grade permanent magnets (PMs) used to manufacture them [5], to mention just a few. To overcome these issues, most researchers have become concerned with the use of nonconventional electrical machines for wind energy drives, e.g., stator-active brushless machines [6].

Manuscript received December 26, 2016; revised March 31, 2017 and May 11, 2017; accepted June 8, 2017. Date of publication June 29, 2017; date of current version December 8, 2017. *(Corresponding author: Udochukwu B. Akuru.)*

U. B. Akuru is with the Department of Electrical and Electronic Engineering, Stellenbosch University, Stellenbosch 7599, South Africa, on leave from the Department of Electrical Engineering, University of Nigeria, Nsukka 410001, Nigeria (e-mail: udochukwu.akuru@unn.edu.ng).

M. J. Kamper is with the Department of Electrical and Electronic Engineering, Stellenbosch University, Stellenbosch 7599, South Africa (e-mail: kamper@sun.ac.za).

Color versions of one or more of the figures in this paper are available online at http://ieeexplore.ieee.org.

Digital Object Identifier 10.1109/TIE.2017.2721928

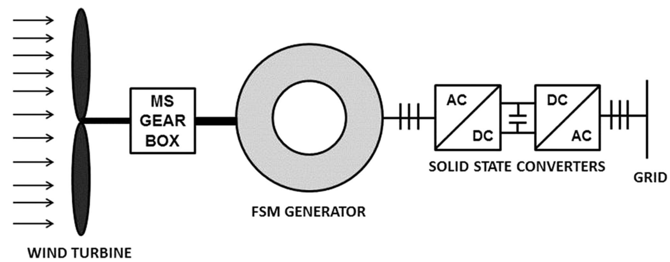

Fig. 1. Proposed geared MS wind energy drive system.

The flux switching machine (FSM) as an example of stator-active brushless machines, recently resurfacing [7], are gradually gaining a foothold in wind energy applications [8]–[14]. Except for [14], the other studies ([8]–[13]) are predominantly PM-FSM options with high-grade PMs and for low-speed systems. On the other hand, there are wound-field (WF) FSM options. The advantage of WF-FSMs over DFIGs is that they do not require slip rings and brushes, and they can be better managed thermally because of the position of their field coils in the stator. With regards to PMSGs and PM-FSMs, WF-FSMs are not only low cost but they allow direct field control.

In this paper, WF-FSM is presented as a suitable candidate for geared medium-speed (MS) wind energy drives, as shown in Fig. 1. In contrast to previous works, the current focus is on the integrated design formulation for constrained multiobjective design optimization (MDO) of these machines. This is due to the fact that the MDO strategy for WF-FSMs is yet to be reported for any combination of machine performance parameters, to the best of the authors' knowledge. For example, in [15] different topologies (12-slot/8-pole, 12-slot/5-pole, 12-slot/7-pole, and 9-slot/5-pole) of the WF-FSM were optimally compared by deterministic optimization method with respect to maximum average torque for high torque density applications, whereas in [16] a proposal is made (without design optimization) to replicate the popular 12-slot/10-pole topology as WF-FSM design in order to illustrate improved field-weakening and comparable torque capabilities. In some of the other studies

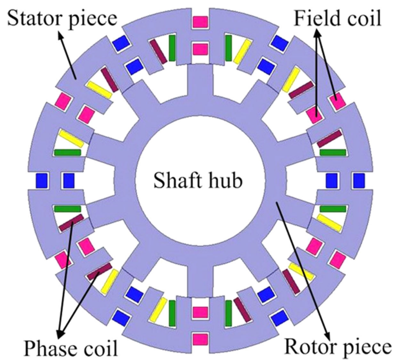

Fig. 2. Cross sections of 12-slot/10-pole WF-FSM topology.

with emphasis on automotive drive applications, the focus is primarily on maximum torque/power capabilities (with/without design optimization) in comparison with PM-FSMs [17]–[20]. Besides, in most of these studies, the articulation of the design process is also not emphasized.

Thus, the current study begins by providing basic information on the initial geometry formulation for WF-FSMs using the popular sizing technique. Thereafter, the MDO process of critical wind generator performance indicators is undertaken using finite-element analyses (FEA) simulations, and based on a preferred stochastic algorithm, which produces a Pareto optimal set. The subsequent sections are used to present the results, discussions, as well as validations, which are based on some chosen optimal design candidates. Finally, the conclusions on the findings are given.

II. WF-FSM Geometry Development

The operating principles of FSMs have been fully represented in the literature [7], [15]–[17], [21]. Generally, FSMs are unique double-salient pole machines with robust rotor structure, having bipolar and sinusoidal phase flux linkages, flux focusing capabilities, and high torque densities [6]. It can be designed to reflect radial [7], transverse [8], or axial flux [9] direction, with the radial-flux design presenting the simplest construction. The most popular radial-flux FSM topology, as shown in Fig. 2, is the 3-phase, 12-slot/10-pole topology, which is primed for this study because of its MS (360 r/min) operating region obtained using

$$n_s = \frac{60 f_e}{N_r} \tag{1}$$

where f_e is the electrical frequency at 60 Hz and N_r is the number of rotor poles. With this generator shaft speed, a low-cost, 1- or 2-stage gearbox, with overall gearbox ratio ranging from 10 to 40, would suffice as a reliable transmission for the turbine rotor to drive the generator shaft.

There is need to also mention that other radial-flux WF-FSM topologies exist as highlighted in [15], but the structure shown in Fig. 2 is without doubt, ahead in terms of optimum phase to field slots combinations per torque density [16]. The design targets for this study are presented, as shown in Table I, for the two different optimization problems envisaged.

TABLE I
Design Requirements

Symbol	Limits	Target 1	Target 2
$\mathcal{P}_{\text{out}}$ (kW)	Output power ≥	10	10
η (%)	Efficiency ≥	88	88
θ_{sF}	Slot fill factor for field windings	0.45	0.45
θ_{sS}	Slot fill factor for phase windings	0.45	0.45
κ_δ (%)	Torque ripple ≤	10	15
pF	Power factor ≥	0.8	0.9

The sizing to power expression developed in [21] for PM-FSMs is given as

$$D_{\text{out}} = \sqrt[3]{\frac{4\tau_e N_s}{\sqrt{2}\pi^2 N_r \kappa_e \kappa_L \Lambda_0^3 A_s \dot{B}_g \eta c_s}} \tag{2}$$

where D_{out} is the stator outer diameter, N_s is the number of slots for the phase windings, κ_e is a factor to account for some leakage, A_s is the electrical loading of the phase windings, $\dot{B}_g$ is the peak airgap flux density, η is the efficiency of the machine, and c_s is the stator tooth arc factor. The electromagnetic torque τ_e, split ratio Λ_0, and aspect ratio κ_L are expressed as

$$\tau_e = \frac{\mathcal{P}_{\text{out}}}{\omega_e}; \quad \Lambda_0 = \frac{D_{\text{in}}}{D_{\text{out}}}; \quad \kappa_L = \frac{l_{\text{st}}}{D_{\text{in}}} \tag{3}$$

where $\mathcal{P}_{\text{out}}$ is the generator outer power, ω_e is the shaft speed in rad/s, l_{st} is the stack length, and D_{in} is the stator interior diameter.

To amend (2) for WF-FSMs, it is required that the sum of both the phase and field electrical loading is given as [22]

$$A_\Sigma = A_s + A_F \tag{4}$$

where A_F is the electrical loading of the field windings, and A_Σ is substituted for A_s in (2).

This done, design parameters such as the stator slot opening width (b_{sls}), stator pole width (b_{ps}), stator yoke height (h_{ys}), rotor pole width (b_{pr}), and rotor yoke height (h_{yr}) are similarly initialized as for PM-FSMs [21], [23], [24]. However, because of absence of PMs, the PM length (b_{pm}) is now replaced with the field core iron length (b_F). Based on the design requirements given in Table I, as well as other sizing parameters, (2) becomes useful to assist the designer in formulating the preliminary dimensions satisfying the design requirements for a typical WF-FSM radial-flux topology.

III. WF-FSM Analytical Modeling

A. Steady-State Equations

To begin with, the proposed MDO will be processed by means of an open-source two-dimensional (2-D) static FEA program called SEMFEM [25], which is then coupled to an optimizer called VisualDoc [26]. Compared with other commercial FEA packages, SEMFEM gives a fast, powerful, and flexible option for the simulation and optimization of electrical machines by the use of Python scripting. In essence, SEMFEM enables the user to analytically solve the steady-state *d–q* equations by simply utilizing the flux linkage results from the FEA program.

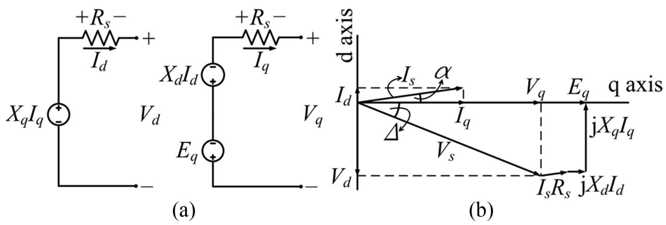

Fig. 3. WF-FSM model: (a) d–q equivalent circuits and (b) phasor diagram.

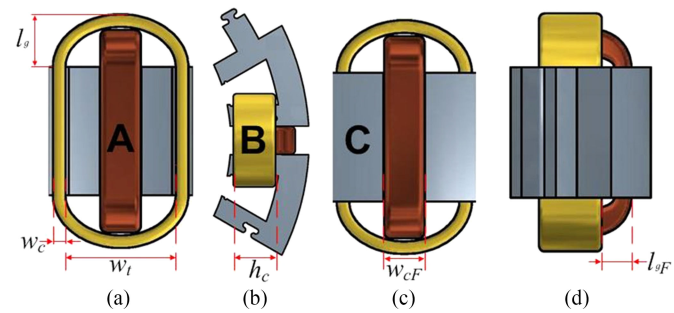

Fig. 4. Different WF-FSM end-winding projection: (a) airgap side, (b) radial cross section, (c) outer perimeter surface, and (d) axial cutout. (Parts: A = field coil, B = phase coil, C = stator laminations.)

To this end, the steady-state direct axis (d-axis) and quadrature axis (q-axis) (a.k.a. d–q axes) equations of the WF-FSM, as evinced from the d–q equivalent circuit and phasor diagrams shown in Fig. 3, are processed via Python scripts so as to improve the speed of the design optimization process. Hence, based on generator mode, the d–q axes voltages are given as

$$V_d = -R_s I_d + X_q I_q \quad (5)$$

$$V_q = -R_s I_q - X_d I_d + E_q \quad (6)$$

where R_s is the phase resistance, X_d and X_q are the d–q axes reactances (sum of the magnetizing, leakage, and end-winding phase reactances, which will be discussed in the subsequent subsection), I_d and I_q are the d–q axes phase currents, and $E_q = -\omega_e \lambda_M$ is the no-load generated voltage, with λ_M being the no-load flux linkage.

The electromagnetic torque and torque ripple are given as

$$\tau_e = \frac{3}{2} N_r \left(I_q \lambda_M + \left(\frac{X_d - X_q}{\omega_e} \right) I_d I_q \right) \quad (7)$$

$$\kappa_\delta = \frac{\tau_{e(\max)} - \tau_{e(\min)}}{\tau_e} \quad (8)$$

where $\tau_{e(\max)}$ and $\tau_{e(\min)}$ are the maximum and minimum fluctuations of τ_e when the machine is on load.

The phase and field resistance are given as

$$R_s = \frac{2qN_{\rm ph}^2 \rho_{\rm Cu} l_{\rm st}}{A_{\rm ph}}, \qquad R_F = \frac{2q_F N_F^2 \rho_{\rm Cu} l_{\rm st}}{A_F} \quad (9)$$

where q and q_F are the respective number of phase and field coils in series connection, $N_{\rm ph}$ and N_F are the respective turns number per coil for the phase and field windings, $\rho_{\rm Cu}$ is the resistivity of copper at 80 °C [17], and $A_{\rm ph}$ and A_F are the areas of the phase and field coils, respectively.

The rms output voltage and current are calculated as

$$V_s = \sqrt{0.5\left(V_d^2 + V_q^2\right)}, \qquad I_s = \sqrt{0.5\left(I_d^2 + I_q^2\right)}. \quad (10)$$

The power, total copper losses, and core losses are given as

$$\mathcal{P}_{\rm out} = \frac{3}{2}\left(V_d I_d + V_q I_q\right) \quad (11)$$

$$P_{\rm Cu} = \frac{3}{2}\left(I_d^2 + I_q^2\right) R_s + I_F^2 R_F \quad (12)$$

$$P_{\rm Core} = C_m f_e^\beta \sum_{k=1}^{N} \dot{B}_k^\sigma M_k \quad (13)$$

where I_F is the field current, C_m, σ, and β are Steinmetz coefficients determined by experiments at different operating frequencies for the iron material, $\dot{B}_k$ is the peak flux density located in the corresponding iron lamination part, M_k is the mass of the corresponding iron lamination stack, and N is the total number of parts considered in the iron lamination.

Thus, the efficiency of the WF-FSM is given as

$$\eta = \frac{\mathcal{P}_{\rm out}}{\mathcal{P}_{\rm out} + P_{\rm Cu+} + P_{\rm Core}}. \quad (14)$$

Finally, the power factor can be evaluated from the load (Δ) and current (α) angles as follows:

$$pF = \cos(\alpha + \Delta) = \cos\left(\tan^{-1}\left(\frac{I_d}{I_q}\right) + \tan^{-1}\left(\frac{V_d}{V_q}\right)\right). \quad (15)$$

B. End-Winding Calculations

The temptation to ignore the end effects in FSMs might arise because in PM-FSMs the end windings are perceived as short. However, the presence and arrangement of the phase coils over the field coils in the WF-FSM topology being considered in this study, makes it necessary to formulate an approximation for the end-winding effects. Moreover, for the sake of the optimization process, an analytical approximation of the end-winding effect is as important as the convergence to the true optimal design. The method of considering only the resistance and ignoring the reactance as done in [15] is unsatisfactory for design optimization process of WF-FSM because at some point in the design space, the end-winding reactance may portend very significant impact on the optimum design. Moreover, prescribing a fixed margin to account for end effects as done in [17] is also limited because the design optimization process of WF-FSMs poses a nonlinear problem. Thus, in this section, the approximate formula proposed for similar nonoverlap PM winding machines in [27] is refined to enable real-time analytic calculations of the WF-FSM end-winding reactance during the design optimization. Calculations for the end-winding resistance are also captured. Initial results are provided to verify the accuracy of the approximations.

Fig. 4 shows how most of the WF-FSM end-winding parameters are devised from different cross-sectional viewpoints. From the preceding subsection, the phase and field resistances, now

TABLE II
ANALYTIC CALCULATIONS VERSUS FEA SIMULATIONS FOR 10 kW WF-FSM

	X_d	X_q	P_{Cu}
3-D FEA	65.493 Ω	64.037 Ω	853.110 W
2-D FEA	57.541 Ω	56.193 Ω	497.102 W
Actual X_e (3-D FEA–2-D FEA)	7.952 Ω	7.844 Ω	356.007 W
Analytic X_e (with $*K_M = 1.5$)	*7.074 Ω	*7.074 Ω	336.691 W
Deviation	11.041%	10.326%	5.425%

with end effects, are recalculated as

$$R_{s(l_{e1}=w_t+2w_c+2l_g)} = 2qN_{\mathrm{ph}}^2\rho_{\mathrm{Cu}}\frac{l_{\mathrm{st}}+l_{e1}}{A_{\mathrm{ph}}} \tag{16}$$

$$R_{F(l_{e2}=2(l_{gF}+w_{cF}))} = 2q_F N_F^2\rho_{\mathrm{Cu}}\frac{l_{\mathrm{st}}+l_{e2}}{A_F} \tag{17}$$

where l_{e1} is the end-winding length on one side of the phase coil, w_t is the average tooth width, w_c is the phase coil width, l_g is the full distance of the phase end-winding from the lamination stack, l_{e2} is the end-winding length on one side of the field coil, l_{gF} is the full distance of the field end-winding coil from the lamination stack, and w_{cF} is the field coil width.

Calculations for the end-winding reactance are reformulated based on the method described in [27] as

$$X_{e(1)(a=0.5l_e,\ b=h_c,\ c=w_c)} = \frac{1.937}{n_a^2}\frac{2a^2}{b}\omega_e N_{\mathrm{ph}}^2 qK \quad (\mu\Omega) \tag{18}$$

$$X_{e(2)(a=0.5l_e,\ b=2w_c,\ c=h_c)} = \frac{1.257l_e}{n_a^2}\frac{2a}{b}\omega_e N_{\mathrm{ph}}^2 qK \quad (\mu\Omega) \tag{19}$$

$$X_e = K_M\left(X_{e(1)} + X_{e(2)}\right) \times 10^{-6} \tag{20}$$

where $l_e = w_t + w_c$, w_t and w_c are as previously defined, h_c is the height of the phase coil, n_a is the number of parallel circuits, and *K* is a constant as described in [27]. The expressions in (18) and (19) are when $l_g >$ 2.5 mm. The variables *a*, *b*, and *c* are used to determine *K*, while K_M is a factor required to account for high mutual phase coupling effects.

It has to be mentioned that the end reactance effect is not applied to the field windings due to the nonperiodic nature of the field current. Also, to establish the accuracy of the emulated analytic expressions for the end effect estimation, the difference between the *d*–*q*-axes reactance in 2-D (without end effects) and 3-D FEA is taken as the actual end-winding inductance. Thus, for a random 10 kW WF-FSM sample design, the actual versus analytic evaluations as devised in (16), (17), and (20) are compared in Table II. The copper losses as compared are in terms of the total end-winding losses. Although the analytic formulations fall behind by some margins when compared to the actual 3-D effects, the approximation is nevertheless beneficial in terms of speed and nonlinearity for the proposed WF-FSM MDO problem.

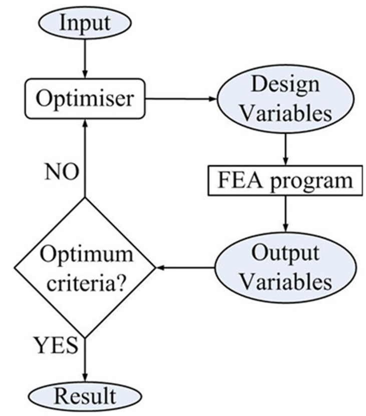

Fig. 5. Flowchart for WF-FSM design optimization.

IV. MULTIOBJECTIVE DESIGN OPTIMIZATION

A. Optimization Procedure and Problem Formulation

The design optimization of electrical machines is a nonlinear process [28], which leads to discontinuity for gradient-based (deterministic) solutions. Hence, a constrained non-gradient multiobjective approach presents the best solution for any given problem because it allows each objective to formulate the right partnership (compromise) in the final optimum design. The basic outcome of such design optimization process is a set of optimal solutions known as the Pareto optimal set.

A number of objectives that may be sought for in the design optimization of wind generators include maximum power factor, minimum torque ripple, and lowest cost or minimum mass; a combination of these for the design optimization of WF-FSMs is yet to be reported. In this paper, FEA-based MDO facilitated by analytical formulations is undertaken in a highly efficient evolutional algorithm—the nondenominated sorting genetic algorithm (NSGA-II)—to predict the behavior of WF-FSMs for wind energy drives. The design optimization work-flow process is illustrated in Fig. 5.

NSGA-II is an adaptive search technique inspired from nature and works on the principle of Darwin's theory of the survival-of-the-fittest, otherwise broadly referred to as evolutionary algorithms. It works with a set of solutions (population) and as the simulation (evolution) proceeds, the individuals in the population improve [29]. NSGA-II is a fast and elitist multiobjective algorithm, which works on the principle of nondominated sorting by using two-tier fitness assignment technique—primary and secondary fitness. The primary fitness is evaluated based on domination level, whereas the secondary fitness is evaluated based on the diversity of the solution in its domination level. The two operators used to express domination ranks are crossover probability P_c and mutation probability $P_m = 1/n$ (where *n* is the number of design variables), while the distribution indexes for crossover (η_c) and mutation (η_m) are parameters used for the control of diversity. The highlight of NSGA-II algorithm is that it produces an optimal solution set, whereby none of the solutions in the optimal solution set dominate because they are equally useful to the specific choice of the machine designer. However, it must be said that a major limitation in using NSGA-II algorithm with FEA solution of electrical machines is the huge computation memory and time required for the procedure.

The criteria used to determine the design constraints and set of objectives are incumbent on the proposed application of the WF-FSM design. Thus, to design a suitable wind generator, the following considerations are important.

1) The head mass should be made as light as possible, especially since the presence of the field coils tend to create high split ratios for WF-FSMs [14]. Besides improving the power density of the wind generator, minimizing the generator mass will result in lower manufacturing costs.
2) The field losses in WF-FSM tend to worsen its efficiency performance [14], [17].
3) Because FSMs are generally inverter-fed machines [21], a high power factor is very critical to the size and cost of the solid state converter (SSC), which affects the overall drivetrain.
4) The lowest torque ripple is critical to the survival of the drivetrain, even as they are a source of mechanical stress [30]. Besides, FSMs are generally known to suffer from high torque ripples [6].

Thus, the MDO process is embarked upon in two different problems posed as follows:

$$1: \min \{F(\mathbf{x}) = [M_F(\mathbf{x}),\ M_A(\mathbf{x})],\ \text{s.t.} \{G(\mathbf{x})[\mathcal{P}\text{out}(\mathbf{x}) \geq 10\,\text{kW},\ pF(\mathbf{x}) \geq 0.8, \kappa_\delta(\mathbf{x}) \leq 10\%,\ \eta(\mathbf{x}) \geq 88\%] \tag{21}$$

$$2: \min \{F(\mathbf{x}) = [1/pF(\mathbf{x}),\ \kappa_\delta(\mathbf{x})],\ \text{s.t.} \{G(\mathbf{x})[\mathcal{P}\text{out}(\mathbf{x}) \geq 10\,\text{kW},\ \eta(\mathbf{x}) \geq 88\%] \tag{22}$$

where $F(\mathbf{x})$ is a vector of the objective functions, $G(\mathbf{x})$ is the feasible design space, $\mathbf{x}$ is a vector composition of the design variables, M_F is the field coil mass, and M_A is the active mass.

Equation (21) represents Problem 1, whereas (22) represents Problem 2. In the first MDO problem, the quest is to establish a relationship between the two objectives by minimizing M_F and M_A for a given optimal point such that it satisfies the four performance constraints ascribed to it. Because of issues with hard constraints, which could be occasioned by the highly restricted feasible search region in Problem 1, a second MDO problem is adjudicated such that it relaxes on the masses, but targets an optimum partnership between power factor and torque ripple performance, thus limiting the constraints to only two parameters—output power and efficiency. In summary, the first problem majors on optimizing the cost of the wind generator, whereas the second problem majors on optimizing the cost of the SSCs.

The design variables, describing both dimensional and nondimensional parameters, are given as

$$\mathbf{x} = [\alpha,\ J, J_F, l_{\text{st}}, D_{\text{in}}, D_{\text{sh}}, h_F, b_F, b_{\text{pr}}, b_{\text{sls}}, h_{\text{ys}}, h_{\text{yr}}, t_0] \tag{23}$$

where J and J_F are the phase and field current density, D_{sh} is the rotor shaft diameter, h_F is the field core iron width, and t_0 is a tapering factor for the rotor teeth defined as $b'_{\text{pr}}/b_{\text{pr}}$. The rest of the parameters are as previously defined. In all, 13 design variables are investigated. The geometrical parameters considered for the MDO problems are shown in Fig. 6.

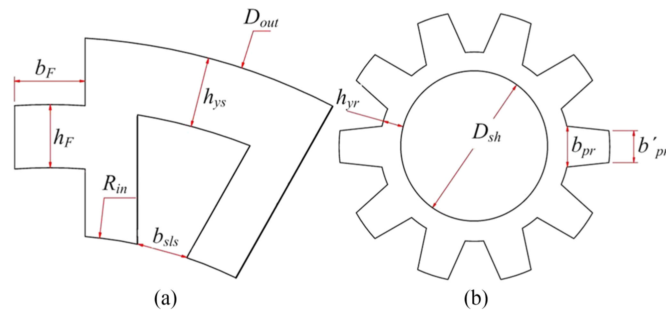

Fig. 6. WF-FSM geometric variables in: (a) stator segment and (b) rotor.

To maintain a realistic search domain during the MDO process, five boundary conditions, which are necessary to harness the dimensional parameters of the WF-FSM, are enumerated sequentially as follows:

$$D_{\text{out}} - D_{\text{in}}^{(U)} > 2h_{\text{ys}}^{(U)} \tag{24}$$

$$D_{\text{out}} - D_{\text{in}}^{(U)} > 2h_F^{(U)} \tag{25}$$

$$\tau_s^{(L)} > b_F^{(U)} + b_{\text{sls}}^{(U)} \tag{26}$$

$$D_{\text{rot}}^{(L)} > D_{\text{sh}}^{(U)} + 2h_{\text{yr}}^{(U)} \tag{27}$$

$$\pi\left(D_{\text{sh}}^{(L)} + 2h_{\text{yr}}^{(L)}\right) > N_r b_{\text{pr}}^{(U)} \tag{28}$$

where superscripts L and U are used to indicate the lower and upper limits of the respective parameter, τ_s is the stator pole pitch, and D_{rot} is the rotor external diameter. Other parameters have been previously defined. The boundary limits for the nondimensional parameters are also imposed to the satisfaction of the design criteria.

The WF-FSM design is optimized to fit a frame size with stator outer diameter fixed at 600 mm, based on estimation from (2). Other parameters that were fixed during the MDO process include the slot fill factor for the phase and field slots, the number of turns for the phase and field slots, as well as the airgap length. Since NSGA-II algorithm is a stochastic process, the initialization of the design variables can be taken at random values that fall inside the boundary limits.

Two different simulation runs are administered on Problem 1, the only difference being in the parameter settings as shown in Table III. All the problems investigated were carried out within the same design space, using similar starting criteria for the design variables. To attain the final optimal solutions, a total 3750, 4000, and 4000 design candidates are evaluated for the problems defined as 1A, 1B, and 2, respectively.

B. Optimization Results and Thoughts

The converged Pareto optimal solutions are shown in Figs. 7–9. The scatter plots (red markers) constitute the feasible search region, whereas the solid concentric circles (blue markers) are the Pareto optimal solutions, which constitute the

TABLE III
NSGA-II PARAMETERS

Parameter	Problems		
	1A	1B	2
Mutation probability, P_m		0.077	
Crossover probability, P_c	0.95	0.9	0.9
Mutation distribution index, η_m	20	10	10
Crossover distribution index, η_c	20	20	20
Populations	25	40	40
Iterations	150	100	100

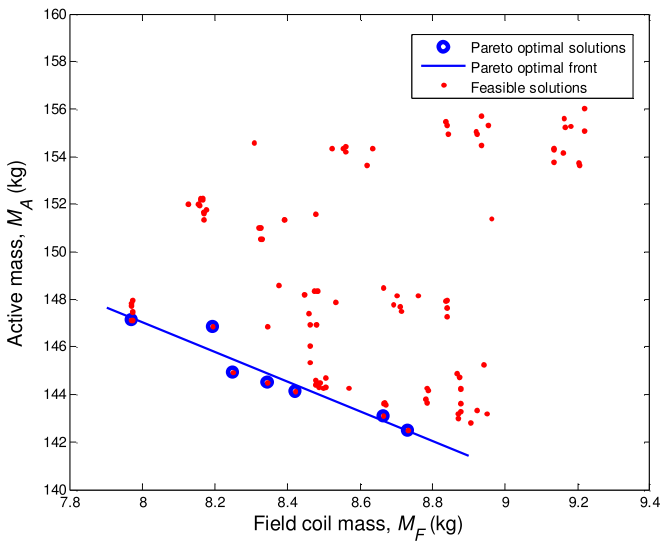

Fig. 7. Obtained Pareto optimal front for Problem 1A.

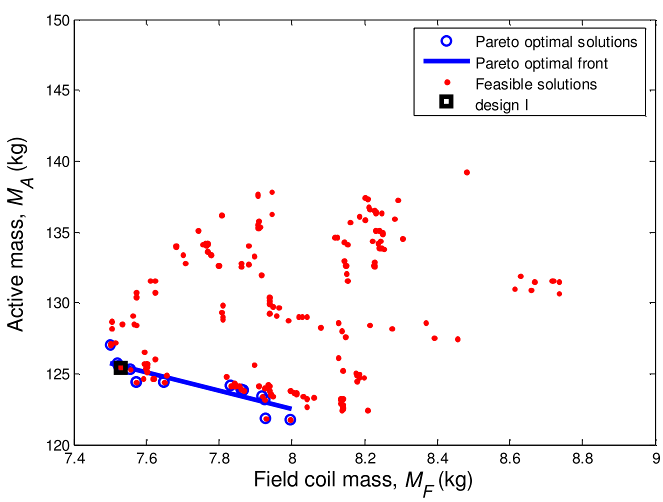

Fig. 8. Obtained Pareto optimal front for Problem 1B.

Pareto optimal front (blue lines). Although a lower population is debuted for Problem 1A compared to Problem 1B, an achievement of wider spread of solutions across the Pareto optimal front is witnessed in the latter because of the smaller distribution index used [29]. Both runs of Problems 1A and 1B show scanty populations due to constraints' violations at 19.3% and 12%, respectively, in the feasible search region. However,

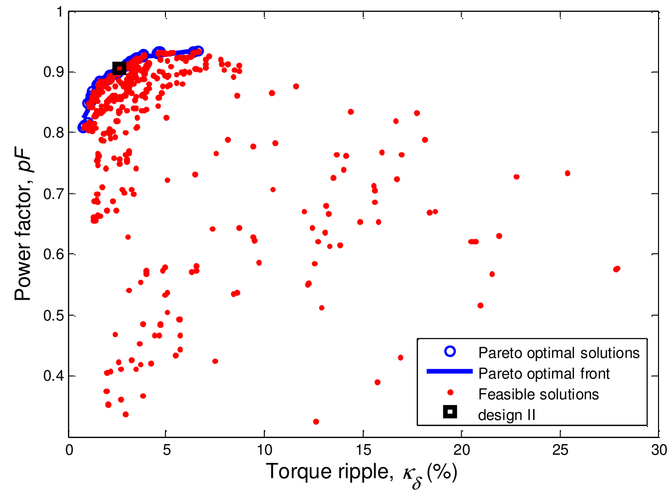

Fig. 9. Obtained Pareto optimal front for Problem 2.

TABLE IV
COMPARISON OF OPTIMAL PERFORMANCE INDICES

Quantity	design I		design II		Deviation*
	Analytic	FEA	Analytic	FEA	
τ_e (Nm)	258.76	258.71	318.99	318.98	23.27%
κ_δ (%)	9.11	34.42	2.56	47.76	−71.89%
$\mathcal{P}_{\text{out}}$ (kW)	10.04	10.01	12.22	12.22	21.71%
η (%)	88.59	88.59	87.92	87.92	−0.75%
pF	0.8	0.78	0.9	0.9	12.50%
M_F (kg)	7.53		11.73		55.77%
M_A (kg)	125.43		201.19		60.40%
τ_e/M_A (Nm/kg)	2.06		1.58		−23.30%
J (A/mm^2)	2.70		2.22		−17.77%
J_F (A/mm^2)	4.98		4.98		0%
X_d (Ω)	40.41		82.98		105.34%
X_q (Ω)	39.24		81.18		106.88%
$^\S s$ (X_d/X_q)	1.02		1.02		0%

*Differences mainly from analytic solutions. $^\S s$ denotes the saliency ratio.

the tradeoff, which exists between the field coil mass and the active mass along the Pareto optimal front, is clearly shown, with Problem 1B presenting the best outcome.

But, Fig. 9 shows that if the mass of the WF-FSM is not prioritized during the MDO process, the power factor can be significantly improved. As indicated along the Pareto optimal front in Fig. 9, significantly higher power factor performance is obtained at lower torque ripple values compared to Problems 1A and 1B shown in Figs. 7 and 8, respectively.

To better appreciate the WF-FSM performance, two selections are made for further evaluation and comparison. As indicated by the points (black square markers) in Figs. 8 and 9, independent selections—designs I and II—are randomly made with emphasis on the "optimum" operating points for the proposed wind generator drivetrain. In Table IV, the selected designs are compared with regards to satisfying the optimal performance criteria, with both the actual FEA as well as the FEA-based analytically formulated results shown. The following inferences are made:

1) Although design II witnessed higher output power compared to design I, its torque density is lesser by 23.3% because the component mass is not minimized.
2) Although the active mass of design I is 60.4% lighter compared to design II, there is no significant advantage in terms of efficiency. Besides, the field to active mass ratio when considered is approximately the same in both optimal design candidates.
3) The power factor in design II compared to design I is superior by 12.5%. In the same token, the torque ripple is significantly lower in the former (–71.8%).
4) Similar to what obtained in [31] for interior permanent magnet (IPM) machines, lower power factor as observed in design I is because of the main objectives that focused on minimum mass. Thus, no clear advantage is achieved in both selected candidates in terms of saliency ratio, which are seen to be identical.
5) For both designs, the major limitation between using actual FEA results to using those calculated from analytic formulations derived from FEA-determined flux linkages is expressed in terms of the torque ripple. This is due to the fact that the torque expression in (7) does not explicitly capture the actual undulation from the on-load airgap field distribution as in a purely FEA case.

In summary, design I presents an optimum solution for minimum size and cost of the proposed wind generator, within the respected performance limits. However, if the cost of the generator is not prioritized during the design optimization stage, then another optimum design can be attained whereby the performance of the generator may result in smaller kVA ratings in respect to cost savings for the SSC. To explain this phenomenon, it is understandable that in the case of design I, a higher level of restraint is experienced with regards to the electromagnetic performance because of the greater number of performance constraints required to achieve minimum generator mass *vis-à-vis* manufacturing costs.

C. 3-D FEA Evaluation

Insofar as this study is based on 2-D magnetostatic FEA solutions aided by analytical formulations, this section discusses additional evaluations performed in 3-D transient FEA simulations using ANSYS Maxwell. To this end, Problem 2 is repeated, but this time the torque, together with the torque ripple, is exclusively evaluated in 2-D FEA, while other performance parameters (power factor and efficiency) still follow from the FEA cum analytic formulations. The only alteration done in this case is in respect of the NSGA-II parameter settings shown in Table III by increasing the number of iterations to 125, resulting in a total of 5000 design candidates.

The obtained Pareto front is shown in Fig. 10. As can be seen, the trend is consistent with previous observation in Fig. 9. The fact that, in Fig. 10 compared to Fig. 9, the Pareto front tends to curve further away from the axes peripheral to it, as well as the stretching of both axes in the feasible design space, beyond other factors, is an indication that the torque ripple estimation is underrated in the latter. Based on the new solutions, design III is

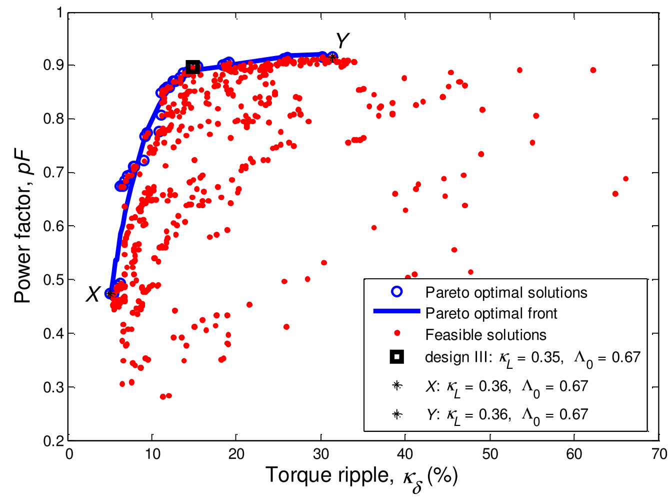

Fig. 10. Obtained Pareto optimal front for Problem 2, showing the torque ripple evaluated from purely 2-D FEA torque output.

selected as indicated in Fig. 10. Also, highlighted in Fig. 10 are the optimal aspect (κ_L) and split (Λ_0) ratios for design III, as well as for the two extreme Pareto optimal solutions highlighted in points "X" and "Y." Not much difference is observed in the values when compared for κ_L and Λ_0, because the stator outer diameter is kept constant.

In Fig. 11, the highlighted design points in Fig. 10 are contrasted in order to emphasize key design variables affected in relation to the technique adopted for design II. It can be seen that the design parameters heavily affected in design III are primarily related to the rotor or airgap such as $b_{\rm pr}$, $b_{\rm sls}$ and $h_{\rm yr}$, with the exception of h_F and J, which are mainly stator parameters. This is due to slot effects and a double salient structure, critical to the torque ripple. Unlike what obtained when κ_L and Λ_0 are compared for the design points "X" and "Y," the design parameters, J and α, among others, significantly influences the extreme outcomes. Considering the phasor diagram for the WF-FSM generator shown in Fig. 3(b), it becomes understandable why the power factor at point "X" is compromised.

To further emphasize the cost implication, M_F and M_A for design III is 14.85 and 198.54 kg, respectively. By comparing values of design III to those of design II (see Table IV), the ratio M_F/M_A yields 7.47% and 5.83%, respectively. This is because the technique used in realizing design III seriously impedes the power factor (see Fig. 10), thus requiring extra field current by decreasing J_F and h_F, as shown in Fig. 11.

Based on requirements set forth in Table I, the obtained 2-D results for design III are verified in 3-D. The magnetic field and flux line distributions in 2-D and 3-D are shown in Fig. 12. Table V, which displays the comparative performance, shows good agreement, except for the κ_δ, which is likely because of coarse meshing used in 3-D. Note that the higher values recorded in 3-D for τ_e cum $\mathcal{P}_{\rm out}$ is because only τ_e and κ_δ are evaluated strictly with 2-D FEA, whereas other performance parameters are evaluated analytically as previously evinced. The higher η recorded in 3-D as opposed to 2-D is because of the remarkable difference in $P_{\rm Core}$, as shown in Table V. In particular, the

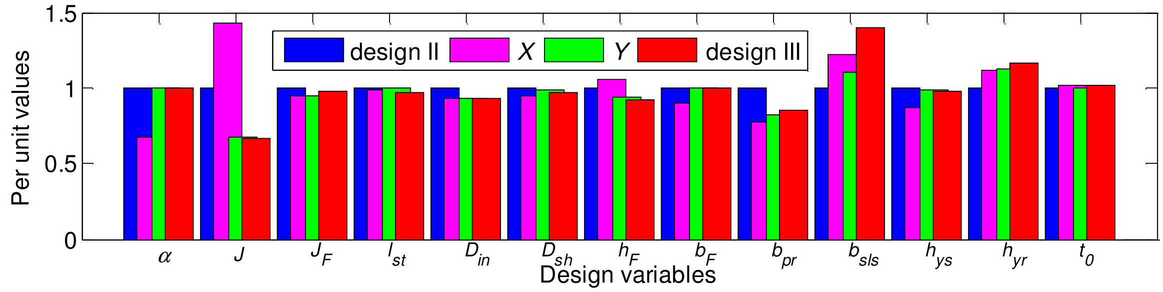

Fig. 11. Per unit values of four optimum WF-FSMs selected from Problem 2 along the Pareto front.

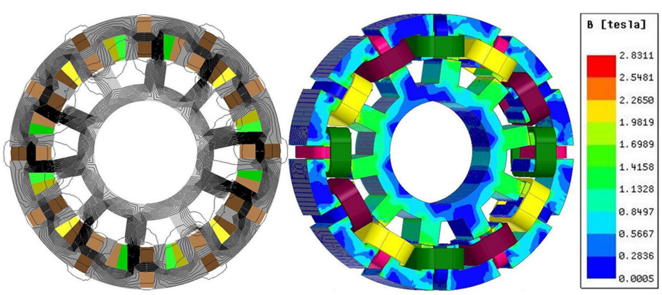

(a) (b)

Fig. 12. FEA plot of: (a) magnetic fields in 2-D magnetostatic solution and (b) flux density surface map in 3-D transient solution.

TABLE V
VALIDATION OF OPTIMAL PERFORMANCE INDICES FOR DESIGN III

Performance quantity	FEA		Deviation
	2-D static	3-D transient	
Electromagnetic torque, τ_e (Nm)	321.43	329.87	2.55%
Torque ripple, κ_δ (%)	14.80	25.58	42.12%
Output power, $\mathcal{P}_{\text{out}}$ (kW)	12.89	13.07	1.37%
Power factor, pF	0.89	0.87	−2.29%
Copper loss, P_{Cu} (kW)	1.329	1.326	−0.22%
Core loss, P_{Core} (kW)	0.464	0.303	−53.13%
Efficiency, η (%)	87.78	88.67	−1.00%

discrepancy in P_{Core} is due to the lower average flux density observed in 3-D along the axial length of the lamination stack compared to 2-D. This characteristic is similar to the PM end-flux fringing effects reported in [27].

V. Conclusion

In this paper, constrained MDO was administered to the 12-slot/10-pole WF-FSM topology and designed for geared MS wind energy drives. Using 2-D FEA-based formulations with a nongradient optimization algorithm, the production of a Pareto optimal solution set was achieved. Two problems were defined for the MDO process, such as Problem 1: to minimize both the field copper and the active mass; and Problem 2: to minimize torque ripple while maximizing power factor. Problem 1 having two separate runs revealed the tradeoff existing between the field coil mass and the active mass along the Pareto optimal front, whereas Problem 2 showed, for the first time, that achieving high power factor results in high torque ripple. Thus, by isolating two optimal design candidates, one from each problem, the importance in approaching the MDO problem from either a manufacturing or performance constraints' viewpoint becomes obvious. When restricted to the same design environment, the WF-FSM performance is constrained if the MDO problem is solely pursued in terms of minimizing the cost of materials. On the other hand, approaching the MDO problem from a solely performance viewpoint could result in beneficial handouts to the overall wind generator drivetrain, such that it lead to minimum kVA rating and cost for the SSC.

Although the 2-D/3-D FEA validation showed good agreement, the potential limitation of using simplified analytical formulations, based on *d–q* flux linkages from static 2-D FEA, was that it oversimplifies the torque ripple calculations.

Acknowledgment

The authors are grateful to K. Cloete of the Electrical Machines Laboratory, Stellenbosch University, for providing some of the sketches used.

References

[1] REN 21, Renewables 2016 Global Status Report (Paris: REN21 Secretariat), 2016. [Online]. Available: www.ren21.net/gsr

[2] A. M. El-Refaie, "Growing role of electrical machines and drives in electrification," in *Proc. 22nd Int. Conf. Elect. Mach.*, Lausanne, Switzerland, 2016, pp. 364–370.

[3] U. B. Akuru and M. J. Kamper, "Contemporary wind generators," *J. Energy Southern Africa*, vol. 26, no. 3, pp. 116–124, Aug. 2015.

[4] H. Polinder, J. A. Ferreira, B. B. Jensen, A. B. Abrahamsen, K. Atallah, and R. A. McMahon, "Trends in wind turbine generator systems," *IEEE J. Emerg. Sel. Topics Power Electron.*, vol. 1, no. 3, pp. 174–185, Sep. 2013.

[5] Z. Q. Zhu and J. Hu, "Electrical machines and power-electronic systems for high-power wind energy generation applications: Part II—power electronics and control systems," *COMPEL Int. J. Comput. Math. Elect. Electron. Eng.*, vol. 32, no. 1, pp. 34–71, 2013.

[6] M. Cheng, W. Hua, J. Zhang, and W. Zhao, "Overview of stator-permanent magnet brushless machines," *IEEE Trans. Ind. Electron.*, vol. 58, no. 11, pp. 5087–5101, Nov. 2011.

[7] S. E. Rauch and L. J. Johnson, "Design principles of flux-switching alternators," *Amer. Inst. Elect. Eng. Trans.*, vol. 74, no. 3, pp. 1261–1268, 1955.

[8] O. Dobzhanskyi, P. Gottipati, E. Karaman, L. Xiaozhong, E. A. Mendrela, and A. M. Trzynadlowski, "Multilayer-winding versus switched-flux permanent-magnet ac machines for gearless applications in clean-energy systems," *IEEE Trans. Ind. Appl.*, vol. 48, no. 6, pp. 2296–2302, Nov./Dec. 2012.

[9] M. Lin, L. Hao, X. Li, X. Zhao, and Z. Q. Zhu, "A novel axial field flux-switching permanent magnet wind power generator," *IEEE Trans. Magn.*, vol. 47, no. 10, pp. 4457–4460, Oct. 2011.

[10] C. Ditmanson, P. Hein, S. Kolb, J. Mölck, and S. Bernet, “A new modular flux-switching permanent-magnet drive for large wind turbines,” *IEEE Trans. Ind. Appl.*, vol. 50, no. 6, pp. 3787–3794, Nov./Dec. 2014.

[11] L. Shao, W. Hua, N. Dai, M. Tong, and M. Cheng, “Mathematical modeling of a 12-phase flux-switching permanent-magnet machine for wind power generation,” *IEEE Trans. Ind. Electron.*, vol. 63, no. 1, pp. 504–516, Jan. 2016.

[12] J. Ojeda, M. G. Simoes, L. Guangjin, and M. Gabsi, “Design of a flux switching electrical generator for wind turbine systems,” *IEEE Trans. Ind. Appl.*, vol. 48, no. 6, pp. 1808–1816, Dec. 2012.

[13] U. B. Akuru and M. J. Kamper, “Evaluation of flux switching PM machines for medium-speed wind generator drives,” in *Proc. IEEE Energy Convers. Congr. Expo.*, Sep. 20–24, 2015, pp. 1925–1931.

[14] U. B. Akuru and M. J. Kamper, “Performance comparison of optimum wound-field and ferrite PM flux switching machines for wind energy applications,” in *Proc. 22nd Int. Conf. Elect. Mach.*, Lausanne, Switzerland, 2016, pp. 2478–2485.

[15] Y. J. Zhou and Z. Q. Zhu, “Comparison of wound-field switched-flux machines,” *IEEE Trans. Ind. Appl.*, vol. 50, no. 5, pp. 3314–3324, Sep./Oct. 2014.

[16] Y. Tang, J. J. H. Paulides, T. E. Motoasca, and E. A. Lomonova, “Flux-switching machine with DC excitation,” *IEEE Trans. Magn.*, vol. 48, no. 11, pp. 3583–3586, Nov. 2012.

[17] T. Raminosoa *et al.*, “Reduced rare-earth flux-switching machines for traction applications,” *IEEE Trans. Ind. Appl.*, vol. 51, no. 4, pp. 2959–2971, Aug. 2015.

[18] Y. Tang, E. Ilhan, J. J. H. Paulides, and E. A. Lomonova, “Design considerations of flux-switching machines with permanent magnet or DC excitation,” in *Proc. 15th Eur. Conf. Power Electron. Appl.*, Sep. 2–6, 2013, pp. 1–10.

[19] E. B. Sulaiman, T. Kosaka, and N. Matsui, “Design study and experimental analysis of wound field flux switching motor for HEV applications,” in *Proc. 20th Int. Conf. Elect. Mach.*, Sep. 2–5, 2012, pp. 1269–1275.

[20] T. Kosaka, N. Matsui, Y. Kamada, and H. Kajiura, “Experimental drive performance evaluation of high power density wound field flux switching motor for automotive applications,” in *Proc. 7th IET Int. Conf. Power Electron., Mach. Drives*, Apr. 8–10, 2014, pp. 1–6.

[21] H. Wei, C. Ming, Z. Q. Zhu, and D. Howe, “Design of flux-switching permanent magnet machine considering the limitation of inverter and flux-weakening capability,” in *Proc. 41st IEEE IAS Annu. Meet. Conf. Rec.*, Tampa, FL, USA, 2006, vol. 5, pp. 2403–2410.

[22] S. Huang, J. Luo, F. Leonardi, and T. A. Lipo, “A general approach to sizing and power density equations for comparison of electrical machines,” *IEEE Trans. Ind. Appl.*, vol. 34, no. 1, pp. 92–97, Jan./Feb. 1998.

[23] Z. Q. Zhu, Y. Pang, J. T. Chen, Z. P. Xia, and D. Howe, “Influence of design parameters on output torque of flux-switching permanent magnet machines,” in *Proc. IEEE Veh. Power Propulsion Conf.*, Sep. 3–5, 2008, pp. 1–6.

[24] L. E. Somesan and I. A. Viorel, “Permanent magnet flux-switching machine, optimal design and performance analysis,” *Adv. Elect. Eng.*, vol. 11, no. 2, pp. 46–53, 2013.

[25] S. Gerber, “A finite element based optimisation tool for electrical machines,” M.Sc. thesis, Dept. of Electr. and Electron. Eng., Stellenbosch Univ., Stellenbosch, South Africa, Mar. 2011.

[26] VisualDOC User’s Manual, Vanderplaats Research & Development, Inc., Colorado Springs, CO, USA, 2006.

[27] J. H. J. Potgieter and M. J. Kamper, “Calculation methods and effects of end-winding inductance and permanent-magnet end flux on performance prediction of nonoverlap winding permanent-magnet machines,” *IEEE Trans. Ind. Appl.*, vol. 50, no. 4, pp. 2458–2466, Aug. 2014.

[28] Y. Duan and D. M. Ionel, “A review of recent developments in electrical machine design optimization methods with a permanent-magnet synchronous motor benchmark study,” *IEEE Trans. Ind. Appl.*, vol. 49, no. 3, pp. 1268–1275, May/Jun. 2013.

[29] K. Deb, A. Pratap, S. Agarwal, and T. Meyarivan, “A fast and elitist multiobjective genetic algorithm: NSGA-II,” *IEEE Trans. Evol. Comput.*, vol. 6, no. 2, pp. 182–197, Apr. 2002.

[30] Y. Y. Xia, J. E. Fletcher, S. J. Finney, K. H. Ahmed, and B. W. Williams, “Torque ripple analysis and reduction for wind energy conversion systems using uncontrolled rectifier and boost converter,” *IET Renewable Power Gener.*, vol. 5, no. 5, pp. 377–386, Sep. 2011.

[31] P. Zhang, D. M. Ionel, and N. A. O. Demerdash, “Saliency ratio and power factor of IPM motors with distributed windings optimally designed for high efficiency and low-cost applications,” *IEEE Trans. Ind. Appl.*, vol. 52, no. 6, pp. 4730–4739, Dec. 2016.

Udochukwu B. Akuru (M’13) was born in Lagos, Nigeria, on June 6, 1983. He received the B.Eng. and M.Eng. degrees in electrical engineering from the University of Nigeria, Nsukka, Nigeria, in 2008 and 2013, respectively. He is currently working toward the Ph.D. degree in electrical machines (renewable energy option) at Stellenbosch University, Stellenbosch, South Africa.

He is a Lecturer with the University of Nigeria, but is currently on leave. His research interests include electrical drives and renewable energy.

Mr. Akuru is a registered member of the Council for the Regulation of Engineering, Nigeria, member and volunteer to IEEE societies, committees and groups, and also serves as a reviewer to major IEEE conferences and transactions.

Maarten J. Kamper (SM’08) received the M.Sc. (Eng.) degree in engineering and the Ph.D. degree in electrical engineering from the University of Stellenbosch, Stellenbosch, South Africa, in 1987 and 1996, respectively.

Since 1989, he has been a Member of Staff of the Department of Electrical and Electronic Engineering, University of Stellenbosch, where he is currently a Professor of electrical machines and drives. His research interests include computer-aided design and control of reluctance, permanent magnet, and inductance machine drives.

Prof. Kamper is a South African National Research Foundation Supported Scientist and a Registered Professional Engineer in South Africa.